Tribology Letters (2023) 71:91
https://doi.org/10.1007/s11249-023-01755-y

ORIGINAL PAPER

Yarn/Yarn Friction Analysis Considering the Weaving Process of Textile Fabrics: Analytical Model and Experimental Validation

Yu Wang[1,2,3,4] · Yanan Jiao[1,2] · Peng Wang[3,4]

Received: 11 April 2023 / Accepted: 24 June 2023 / Published online: 20 July 2023

Abstract

The friction between twisted yarns during the process of manufacturing textile reinforcements has been considered an important issue that can strongly influence the mechanical properties of the preform, which deteriorate the mechanical characteristics of fiber-reinforced composites if the friction is excessive. Based on Hertzian contact theory, a novel analytical model has been developed in this research to describe the friction behavior between the twisted yarns in orthogonal and non-orthogonal contact. The realistic contact area was modeled under micro/meso scales taking into account the contact angle between the yarns and the orientation of the fibers influenced by the twist. The efficacy of the developed model was confirmed by the experimental approach. Through the developed model, the yarn/yarn friction behaviors were characterized under different conditions considering the weaving process, such as orthogonal and non-orthogonal contact, same/different twist level, and same/different twist direction, which is essential for optimizing the textile preform forming process and enhancing the mechanical properties of the composites.

Keywords Micro–meso scale · Fabrics/textiles · Twisted yarns · Friction modeling · Contact mechanism

Nomenclature

F_f	Friction force (N)
COF	Coefficient of friction
$A_{r/yarn}$	Realistic contact area of yarn (m^2)
$A_{r/fiber}$	Realistic contact area of fiber (m^2)
F_n	Normal load in $\vec{n}$ (N)
F_t	Tangential load of yarn (N)
α	Angle between fiber axes (°)
β	Angle between yarn axes (°)
γ	Twist angle of yarn (°)
θ	Angle between $z\left(\vec{z}\right)$ and normal $\left(\vec{n}\right)$ directions (°)
r_f	Radius of fiber (m)
R	Radius of yarn (m)
R^*	Equivalent radius of fiber (m)
E^*	Equivalent Young's modulus of fiber (Pa)
E	Young's modulus of fiber (Pa)
ν	Poisson's ratio of fiber
R'	Major relative radius of curvature of the contact surface
R''	Minor relative radius of curvature of the contact surface
τ	Shear strength (Pa)
H	Displacement under the action of F
f_N	Normal load of fiber (N)
n	Number of contact fibers in width of upper yarn
m	Number of contact fibers in width of lower yarn
T_t	Twist of yarn (tpm)
h_i	Distance between the fibers (m)
b	Half-width of the contact (m)
E_l	Longitudinal modulus of yarn (Pa)
E_t	Transverse modulus of yarn (Pa)
v_{12}	Poisson's ratio of yarn
F	Applied normal force in $\vec{z}$ (N)
F_p	Pre-tension of yarn (N)
l	Length of twisted yarn sample (m)
k	Fitting coefficient
a	Span of sample (m)
u	Distance between contact point and center of span (m)

✉ Peng Wang
peng.wang@uha.fr

[1] Ministry of Education Key Laboratory of Advanced Textile Composite Materials, Tiangong University, Tianjin 300387, China

[2] School of Textile Science and Engineering, Tiangong University, Tianjin 300387, China

[3] Lpmt, Ensisa, University of Haute-Alsace, 68000 Mulhouse, France

[4] University of Strasbourg, Strasbourg, France

1 Introduction

Fiber-reinforced composites are widely used in the aerospace, automotive, ballistics, and protective clothing field because of their high specific strength, high specific modulus, and strong designability [1–3]. The mechanical properties of textile reinforcements, as a significant component, has a decisive effect on the mechanical properties of final composite products [4, 5]. The mechanical behavior of textile reinforcements depends strongly on the yarn-level factors, which are guided by fiber-level interactions [6–8]. Thus, the research on the mechanical properties of fiber and yarn is quite meaningful to develop fiber-reinforced composites [9, 10]. In addition, the damage between yarns will be aggravated during the weaving process, particularly the damage between warp and weft yarns, binder and weft yarns during three-dimensional (3D) orthogonal weaving, whose difference is contact mode, and which generally can be classified according to various contact angles between yarns in the plane coordinate system, namely the orthogonal and non-orthogonal. The typical damage behaviors are illustrated in Fig. 1, which appear mainly in the weaving and beating phases. The contact angle between the weft and warp shows a normal distribution, that is, the yarns of the central part are in orthogonal contact otherwise non-orthogonal contact. Approximately 5–30% of the mechanical strength is lost during weaving as a result of friction, compression, and bending [11–13], with friction accounting for as much as 9–12% of the total loss [14, 15]. Therefore, it is necessary to focus on the research on the friction characteristics of fiber or yarn during the weaving process for composite forming [16–18].

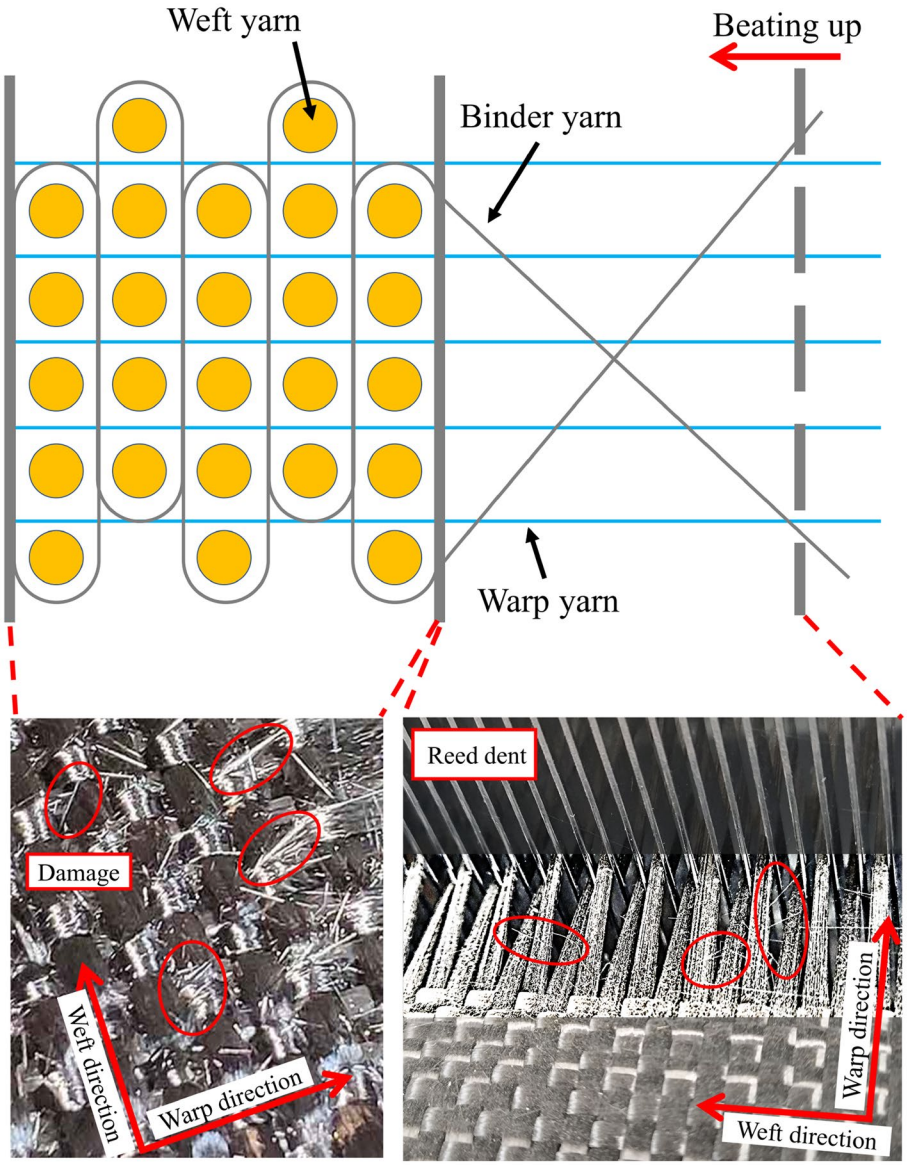

Fig. 1 Example of the yarns' damage formed during 3D orthogonal weaving process [36]

Research on friction of fibers or yarns started in the middle of the twentieth century, with several research teams in the textile field proposing different methods of measurement [19, 20]. At present, the commonly used research methods for fiber or yarn friction include the pull-out method [21, 22], the capstan method [23, 24], the yarn twist method [25, 26], the rotation reciprocating friction method [27–29], and the linear reciprocating friction method [20, 27, 30]. These methods are characterized by a wide range of applications and high accuracy. In addition, to accommodate friction behavior under special working conditions, Tourlonias et al. [29] focused on the friction interactions that occur between yarns and designed a kinematic experiment to simulate the weaving movement of yarns. The results obtained show that the coefficient of friction (*COF*) decreases with the increase in normal load but is not influenced by the oscillation frequency. Ismail et al. [31] worked on the question of fiber-on-fiber dynamic friction, including an experimental set-up and analytical method, to investigate the friction behavior between single fibers under the influence of a pre-tension, which reveals that elastic deformation of the contact prevails over the 'wrapping effect,' generating the contact area over which the interfacial shear takes place. The work mentioned is based on the principle of rubbing one fiber against another fiber in a linear motion to measure [32, 33]. Nevertheless, to the best of the author's knowledge, the effect of twist on friction behavior under dissimilar pre-tension and normal loads has not yet been discussed systematically for detail parameters at the microscale, such as the width of contact, realistic contact area, and number of contact fibers, even though they have been proposed in some classic research [17, 23, 34, 35].

Concerning detail parameters during the friction process, the only few research reported were published for twistless yarns, such as M55JB, T1100 and T300 from Toray [36, 37], and HTS40 from Toho Tenax [27, 38]. Wu et al. [36] established the experimental device and calculated the true number of contact fibers and real contact area based on the Hertzian contact model. The results show that the friction force F versus normal load N_{tow} curves followed power law descriptions, F is proportional to $N_{tow}^{0.734}$ for the investigated carbon tow. Tourlonias et al. [37] studied the influence of the contact angle between two fibers and two tows to understand the evolution obtained by using the adhesion theory of friction from a basic analytical model. The friction behavior is very high when the fibers are parallel, which is due to the large total contact area at 0° and the increase in the adhesion between fibers at the interface of the tows. The real mechanical response of twisted yarns is distinctively dissimilar to twistless yarns, generating the special characteristics during the friction process that are still unclear and need to be realized to achieve a more accurate analytical model.

As mentioned in the literature, research on the friction behavior of yarns needs to disregard the effects of wear, which essentially consists of two concepts in tribology. Hence, ultra-high-molecular-weight polyethylene (UHMWPE) yarns are used to investigate friction behavior without the interference of wear factors due to their excellent wear resistance [39, 40]. Current research aims to investigate the friction behavior of non-parallel conditions between twisted yarns under the influence of a normal load. It is based on classical Hertzian contact theory and adhesion friction theory, a novel approach and analytical methodology for investigating the frictional characteristics of yarns with identical or different twist angles regardless of dissimilar contact angles and twists. Implementing this model also starts with the analysis of fiber–fiber contact, and then utilizes the Hertzian contact theory to describe and calculate the relative parameters during the friction process. To calculate further simply and accurately, more correlated parameters are introduced into this model. Then, the accuracy of this model is validated according to the experimental analysis. Finally, the friction behavior of yarns with the same and different twists is predicted using the model for non-parallel conditions. The friction analysis model we have developed, which takes the twist response into account, could be a bridge linking practical and theoretical analysis, which is essential for optimizing the textile preform forming process and enhancing the mechanical properties of the composites. Moreover, this study presents a novel approach and analytical methodology for investigating the frictional characteristics of yarns with identical or different twist angles. The proposed method not only offers valuable insights into understanding the underlying mechanisms but also establishes a solid basis for future exploration and simulation analysis of intricate coupling systems.

2 Micro–meso Modeling of the Friction Between Non-orthogonal Twisted Yarns

The state of the contact pair is vital for the determination of the friction force of yarn according to the widely accepted adhesion theory of friction [23], which can be explained as Eq. (1):

$$F_f = A_{r/yarn} \times \tau, \tag{1}$$

where $A_{r/yarn}$ is the realistic contact area of yarn and τ is the specific shear strength.

The implementation of a model describing the variation of the realistic contact area should thus specify the crucial parameters for each status of contact pair during yarn friction. In this way, the Hertzian contact theory was usually utilized to develop the current model as shown in Fig. 2,

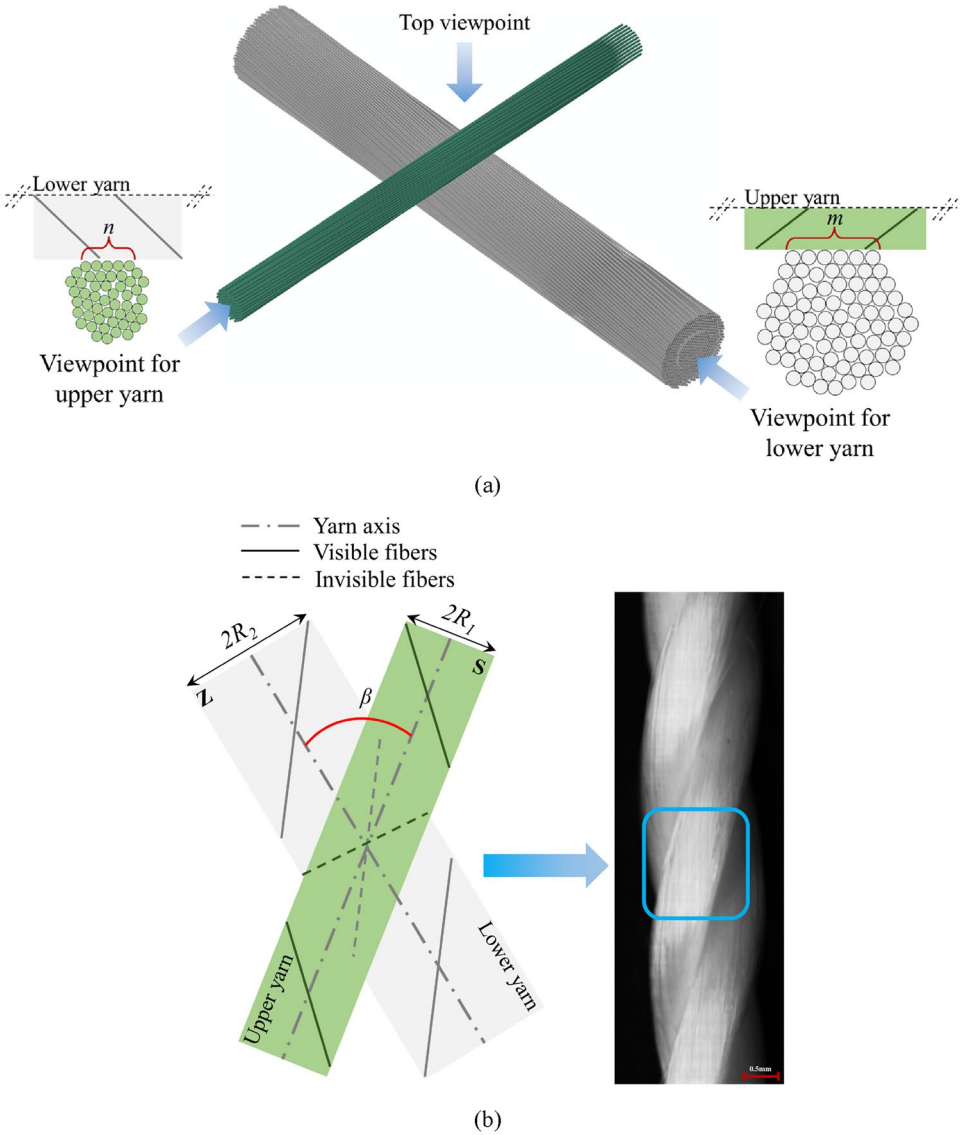

Fig. 2 Schematic diagrams of non-orthogonal contact of twisted yarns: **a** three-dimensional diagram, **b** top viewpoint diagram. (**S** means the direction from upper left to lower right; **Z** means the direction from upper right to lower left)

as it can be used to express the friction behavior of yarns with different twist levels, linear density and twist direction (the orientation of fibers in relation to the yarn axis: S or Z), under different contact angles of yarns.

It is assumed that the arrangement of fiber within yarn is incommensurate, that is, the migration of internal fiber does not take place in a static state, especially after the contact interaction. The relationship between the realistic contact area of fiber ($A_{r/fiber}$) and yarn ($A_{r/yarn}$) can be described in Eq. (2):

$$A_{r/yarn} = (m \times n) \times A_{r/fiber}, \tag{2}$$

where n and m are the numbers of contact fibers in the widths of yarns, which will be shown in Fig. 2. The $A_{r/fiber}$ with a dissimilar contact angle between two fibers has been calculated under the assumption that the fibers are cylindrical [33, 37].

$$A_{r/fiber} = \pi \left(\frac{3 f_N R^*}{4E^*} \right)^{2/3}, \tag{3}$$

where f_N is the normal load of fiber, R^* is the equivalent radius, and E^* is the equivalent Young's modulus expressed as

$$\frac{1}{E^*} = \frac{1 - v_1^2}{E_1} + \frac{1 - v_2^2}{E_2}, \tag{4}$$

where E_1 and E_2 are Young's modulus of two materials rubbing against each other, and v_1 and v_2 are the Poisson's ratio of two materials rubbing against each other. Young's

modulus and Poisson's ratio of fiber are used in this analytical model and are difficult to obtain. Therefore, the values used are averaged from some earlier research [41, 42].

The fibers show an irregular arrangement due to pretension and normal loading. The equivalent radius R^* can be expressed as the following equation:

$$R^* = (R'R'')^{\frac{1}{2}}, \tag{5}$$

where R' and R'' are the major and minor relative radii of curvature on the contact surface, respectively, which can be then possibly obtained by solving Eq. (6) [43].

$$\begin{cases} \frac{1}{R'} + \frac{1}{R''} = \frac{1}{r_{f1}} + \frac{1}{r_{f2}} \\ \frac{1}{R'} - \frac{1}{R''} = \left(\frac{1}{r_{f1}^2} + \frac{1}{r_{f2}^2} + \frac{2\cos(2\alpha)}{r_{f1}r_{f2}} \right)^{\frac{1}{2}}, \end{cases} \tag{6}$$

where r_{f1} and r_{f2} are the radiuses of contact fibers, and α is the contact angle between the axes of fibers.

The equivalent radius R^* that depends on the angle between the yarn axes (β) has been discussed in [37], however, the fibers are not normally parallel to the axis of twisted yarn. To precisely describe the friction behavior between the twisted yarns, the contact angle between the fiber axes (α), the contact angle between the yarn axes (β), the twist level and the twist direction of the yarns are taken into account in this research. Regarding the complexity of the twist, a micro–meso scale analysis needs to be performed.

2.1 Fiber Scale Modeling

The parameters of the fiber scale model, with the contact angle between the two fiber axes and the number of contact fibers as the main parameters, need to be obtained to clarify the parameters of the yarn scale model. The contact angle between the two fiber axes is dissimilar from β between the axes of the two yarns and the twist angle of yarn γ, whose relationships are shown in Fig. 3. At the same time, with different twist directions, α is different and indeed this results in the difference in the realistic contact areas. Therefore, it is important to calculate α by β and γ. In this way, γ should be transformed into a plane coordinate system, however, α needs to be expressed based on the different twist directions by the following equations:

$$\alpha = \begin{cases} -\beta + \gamma_1 + \gamma_2 & S-S \ or \ Z-Z \\ \beta + \gamma_1 - \gamma_2 & S-Z \ or \ Z-S \end{cases} \tag{7}$$

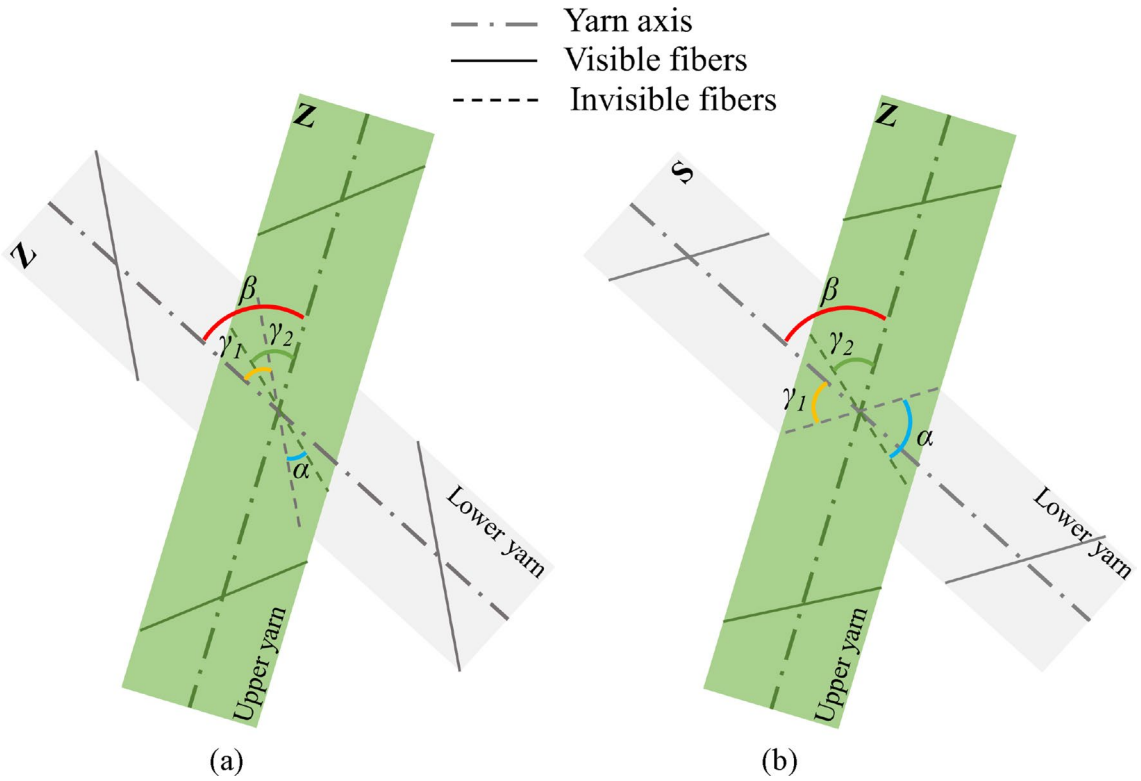

Fig. 3 A diagram of angles analysis during the contact phase of twisted yarns: **a** S–S or Z–Z, **b** S–Z or Z–S

$$\gamma = \arctan 2\pi R T_t, \tag{8}$$

where R and T_t are the radius and twist level of yarn, S–S or Z–Z indicates two S (or Z) yarns in contact, S–Z or Z–S indicates S and Z yarns (or Z and S yarns) in contact.

Then the number of contact fibers n or m (c.f. Fig. 2) of each cross-section of yarn during the friction phase can be expressed as

$$2nr_f + \sum h_i = 2b, \tag{9}$$

where r_f is the radius of fiber, h_i is the distance between two neighboring fibers (see Fig. 4), which can be obtained using the Euclidean distance formula. The half-width of the contact b is vital to calculate n or m under the F_n, as shown in Fig. 4a, which was described by [44] as shown in Eq. (10).

$$b = \sqrt{\frac{8(R^*)^2 F \cdot \cos\theta}{\pi}\left(\frac{1}{E_t} - \frac{v_{12}^2}{E_l}\right)}, \tag{10}$$

where E_l and E_t are longitudinal and transverse moduli of the yarn. v_{12} is the Poisson's ratio of yarn. Based on the assumption of incommensurate structure, the range of n can be given according to the range of h_i. When the distance h_i equals 0, the close homogenous arrangement of fibers is achieved (see Fig. 4b), leading to the number of contact fibers being the maximum at this time, marked as n_{max}. By contrast, when h_i equals $2r_f$, the number of fibers in contact is the minimum, marked as n_{min}, shown in Fig. 4b.

$$n = \begin{cases} \dfrac{b}{r_f} & h_i = 0 \\ \dfrac{2b - \sum h_i - 2r_f}{2r_f} & 0 < h_i < 2r_f \\ \dfrac{1}{2}\left(\dfrac{b}{r_f} + 1\right) & h_i = 2r_f \end{cases} \tag{11}$$

Nevertheless, the situation of the minimum number of fibers cannot be achieved due to the incommensurate arrangement of fiber. When h_i is located in the range $(0, 2r_f)$, the dissimilar h_i is made a summation to calculate n. Since n has a small difference in each section, n is represented by the mean value. Similarly, it is possible to work out the number of contact fibers m in the width of another yarn. Therefore,

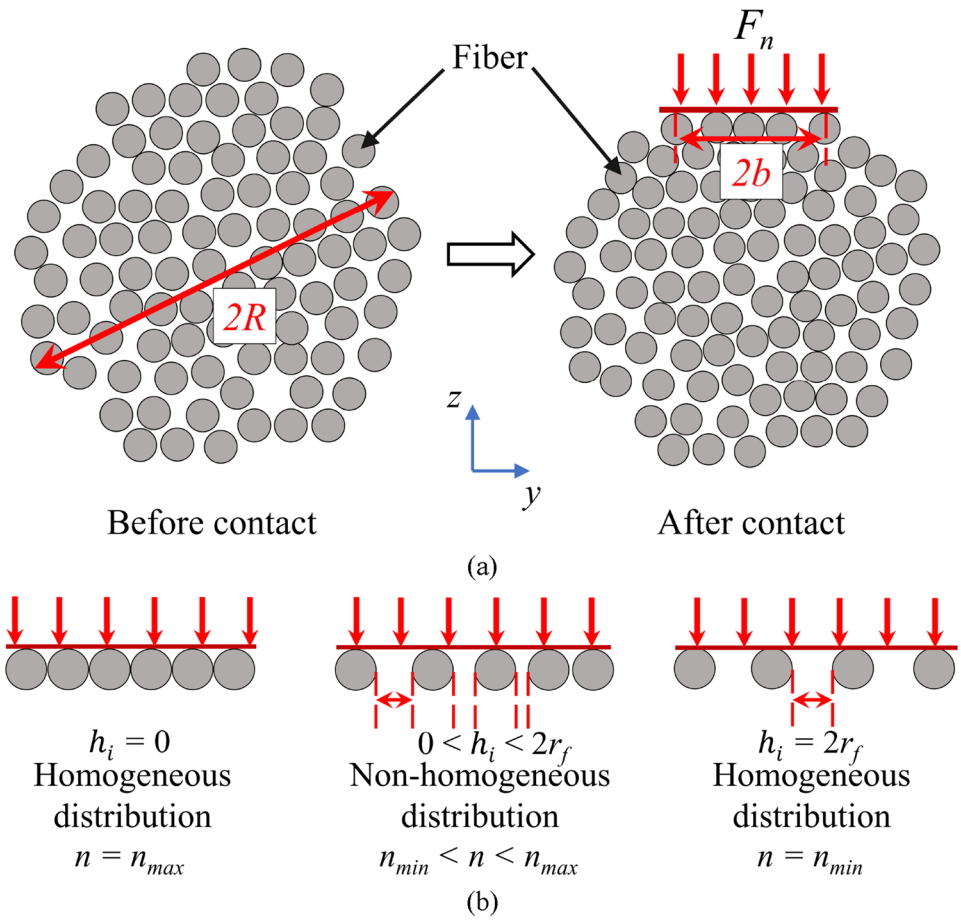

Fig. 4 An enlargement of arrangement to conduct the relation: **a** a deformation description under the normal load F_n and **b** a schema of fiber arrangements (based on the viewpoint in Fig. 2a)

the $A_{r/yarn}$ can be shown, according to the equations above, as a function of the characteristics of the fibers and the contact angle between the fiber axes as described in Eq. (12):

$$A_{r/yarn} = \pi\left(\frac{3r_{f1}r_{f2}\sqrt{mn}\times F\cos\theta}{4}\left(\frac{1-v_1^2}{E_1}+\frac{1-v_2^2}{E_2}\right)\right)^{2/3}\times\left(R'R''-2\cos^2(2\alpha)\right)^{1/3}. \tag{12}$$

2.2 Yarn Scale Modeling

To further describe the friction between the yarns, the parameters at the meso scale must be obtained after the calculation of the realistic contact area of the fibers. The dynamic process needs to be identified, that is, the relationship between F_n and the contact angle between direction of x and yarn (see Fig. 5). In this manner, the normal force F, related to the pre-tension F_p, can be projected in two directions (tangential $\vec{t}$ and normal $\vec{n}$) shown in Fig. 5 and Eq. (13):

$$\begin{pmatrix}F_t\\F_n\end{pmatrix}_{(\vec{t},\vec{n})}=\begin{pmatrix}F\sin\theta\\F\cos\theta\end{pmatrix}, \tag{13}$$

where θ is the contact angle between the directions $\vec{z}$ and $\vec{n}$, which can be characterized by contact angles between the direction x and yarn, F can be expressed in Eq. (14) detailed in "Appendix A":

$$F=\left[E_lS\left(\frac{H}{\sin\theta_1}+\frac{H}{\sin\theta_2}-1\right)+F_p\right]\left(\sin\theta_1+\sin\theta_2\right). \tag{14}$$

The changes in variables a, H, and l had significant effects on. More details of formula derivation are presented in "Appendix A." Thus, an analytical model describing the friction behavior of the yarn (friction force F_f) was established and is shown in Eq. (15).

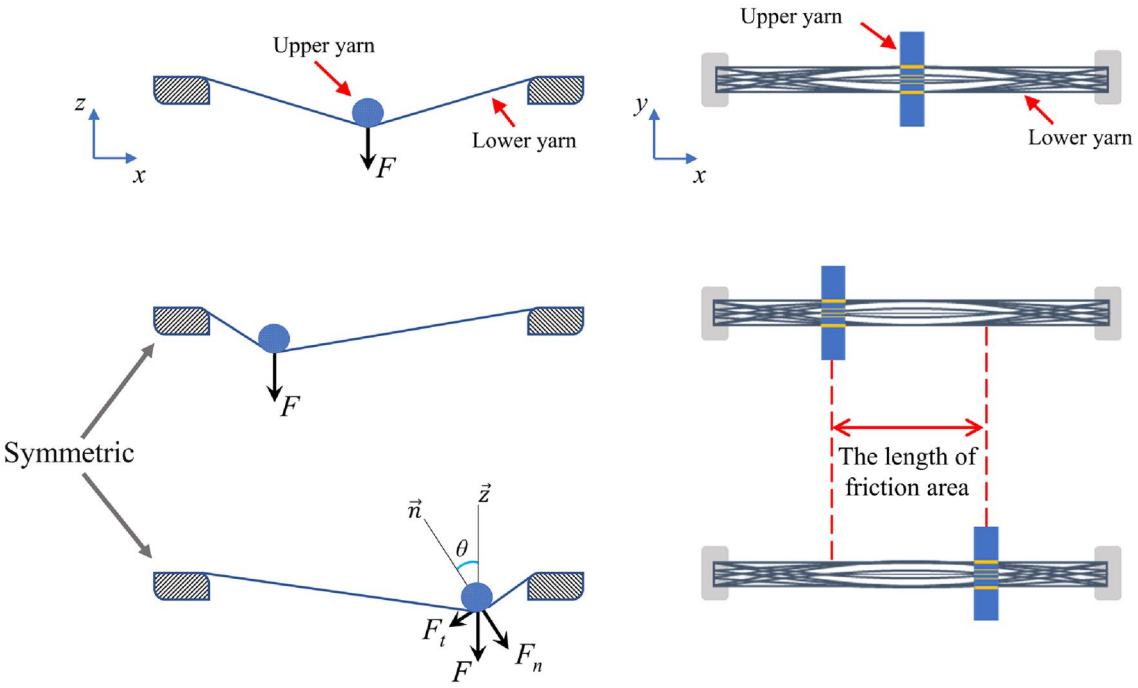

Fig. 5 The kinematic description of the friction process of yarn which includes three characteristic locations where force and contact situation are shown

$$F_f = \pi \sin\theta F^{5/3}\left(\frac{3r_{f1}r_{f2}\sqrt{mn}}{4}\cos\left(\arctan\frac{2H}{a-l\sqrt{\frac{a^2+4H^2-l^2}{a^2-l^2}}}\right)\times\left(\frac{1-v_1^2}{E_1}+\frac{1-v_2^2}{E_2}\right)\right)^{2/3}\left(R'R''-2\cos^2(2\alpha)\right)^{1/3}. \quad (15)$$

The coefficient of friction (*COF*), as an essential parameter of friction behavior, is complicated to obtain since the friction process is dynamic, as shown in Fig. 5. The real-time *COF* needs to be cleared, which was defined as a ratio between the friction force F_f and the normal load F_n at yarn scale in Eq. (16) [33, 37].

$$COF = \frac{F_f}{F_n^k}, \quad (16)$$

where k is the fitting coefficient derived from the experiment, namely 2/3 when the two objects undergo complete elastic deformation.

Table 1 Main physical properties of high-molecular-weight polyethylene (HMWPE) fiber and yarns

Sample	Linear density (Tex)	Twist level (tpm)	Longitudinal modulus (GPa)	Diameter (μm)
Fiber	–	–	0.6	17
Y-50tpm	135(± 2.3)	50	73.0	998
Y-100tpm		100	83.4	493
Y-150tpm		150	98.4	324
Y-200tpm		200	110.3	238

3 Experimental Validation Test

3.1 Materials

The twisted yarns investigated in this article are HMWPE yarns (Spectra®, Honeywell Company, USA). Four yarn samples were prepared and tested for friction. The samples are named according to the twist. For example, Y-50tpm represents the sample of single yarn with 50 tpm (twist per meter). More samples (Y-100tpm, Y-150tpm, and Y-200tpm) are used in the article. For all samples, both yarns were 135 Tex, characterized according to ASTM D 1907/D 1907 M. The main properties related to the tested yarns are noted in Table 1.

3.2 Experiments Set-Up

To confirm the micro–meso model developed in Sect. 2, friction experiments set-up with two specific carriers, including upper and lower carriers, were designed and shown in Fig. 6. The carriages are similar in the upper and lower parts and were designed to fix the sample under a pre-tension load. In addition, some threaded holes were designed to maintain pre-tension of the sample. During the setting up of the sample, one end of the sample is fixed by screwed clamps. The other end of the sample is screwed within the range of a certain pre-tension for a period, with a single fiber pre-tension of at least 0.15 mN per fiber. The fixed part of the sample was protected by a rubber mat [37]. The position should be

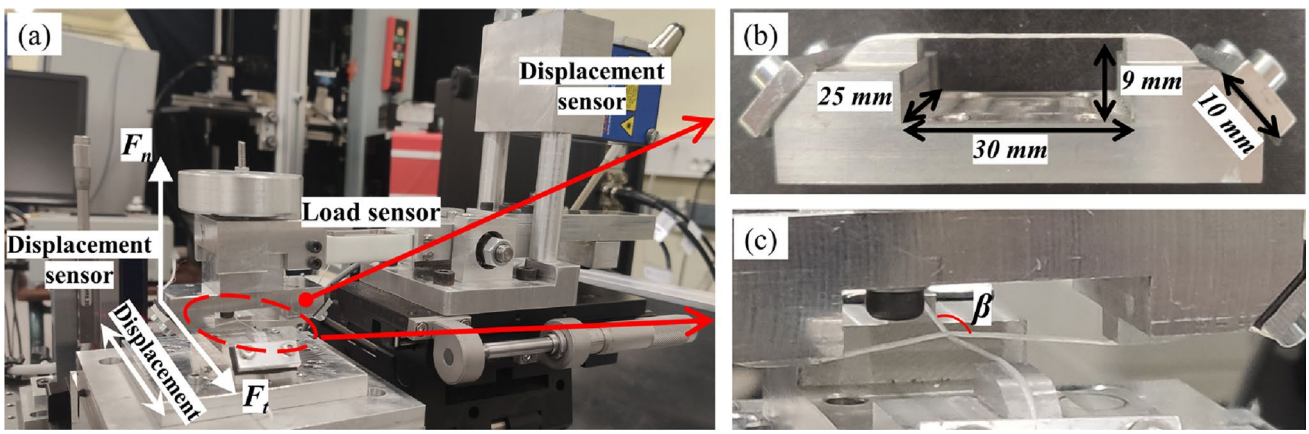

Fig. 6 A picture of the tribometer dedicated to twisted yarn–yarn friction tests

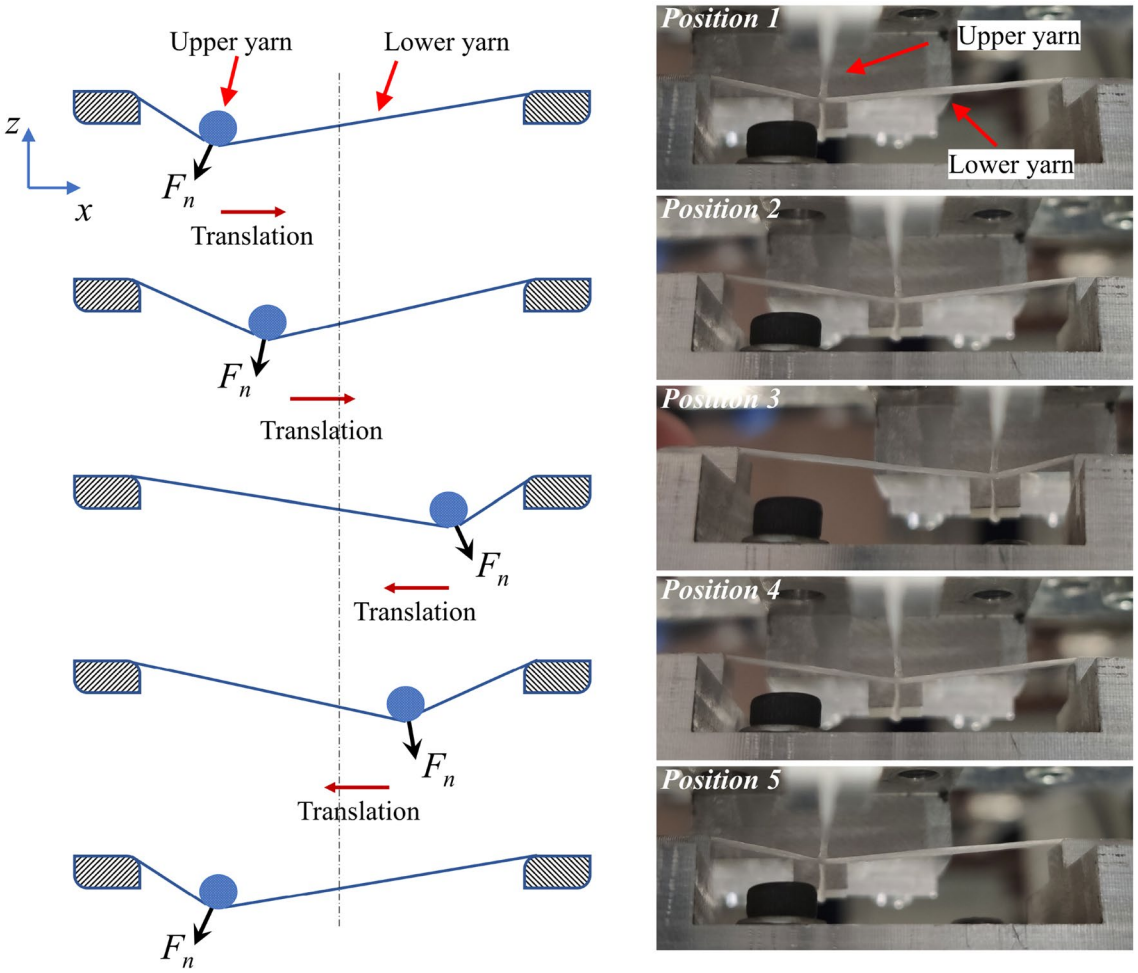

Fig. 7 Schematic diagram of one cycle for the friction test

Table 2 The friction tests with different conditions validate the developed analytical model

Test number	β (°)	Normal force applied (N)	Pre-tension (N)	Twist (tpm)	Twist direction	Cycle number	Sliding distance (mm)	Acceleration (mm/s^2)	Stable velocity (mm/s)
1	90	2.00	0.50	100–200	S–S	20	15	20	10
2	70	1.50	1.00	150–150	S–S				
3	50	1.50	0.35	50–100	Z–S				
4	90	2.00	1.00	200–200	S–S				

such that there is only contact between the upper and lower yarns. The force sensor in Fig. 6 limits the normal load to 20 N and the tangential force to 3 N. The lower carrier is fixed to the base, which is perpendicular to the upper one. This configuration makes it possible to carry out the friction tests for a β of 90°. The length and width of the tested area are chosen as 30 mm and 25 mm (Fig. 6b), which is related to the area in the beating-up. The length of the fixed fiber area is 1 cm, which ensures there is no fiber slippage.

3.3 Experimental Procedure

Once the experiment is set up as shown in Fig. 6, the upper carrier with a force sensor is fixed, and the lower carrier moves reciprocally in the direction of displacement. Figure 7 presents schematically one cycle of the friction test, which starts from an extreme position of the moving carrier (position 1 in Fig. 7). The different normal loads are applied to maintain the contact between the two tested yarns (c.f.

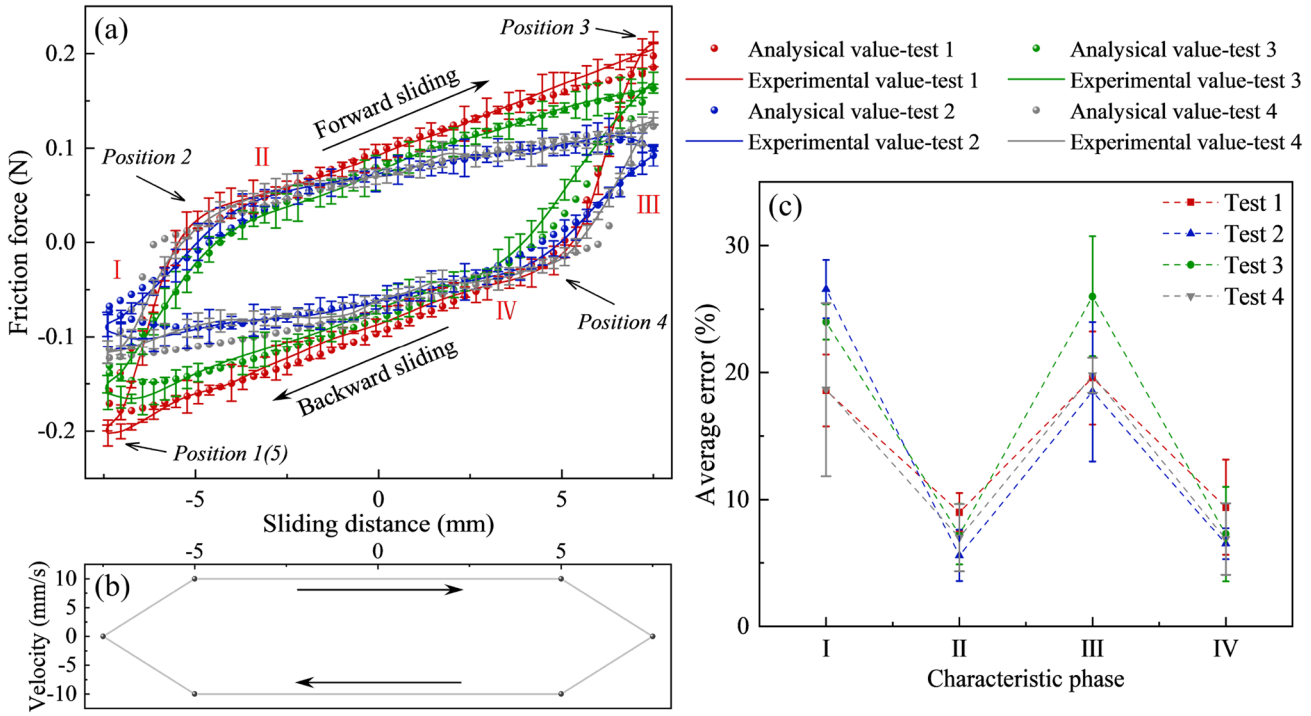

Fig. 8 Comparison of the analytical and experimental results on friction force by different tests mentioned in Table 2 (average of five measurements): **a** one cycle of friction, **b** sliding distance versus velocity curve, and **c** average error of friction force in the characteristic area

Table 2), which were chosen appropriately at the beginning of the test and remained unchanged during the entire friction test.

All experiments were performed at conditions of $22 \pm 2°$ temperature and $65 \pm 4\%$ relative humanity (RH). According to the previous research [31, 37, 45], the weft yarns could be subjected to weaving cycles for 100 mm from the starting position of beating to the fabric (15 mm fabric as an example). Therefore, each test corresponds to 40 friction cycles for each kind of sample under the assumption that there is no secondary friction. The friction tests under different experimental conditions are listed in Table 2.

4 Results and Discussion

4.1 Consistency Analysis of the Friction Response

Based on the analytical model developed in Sect. 2, comparisons were conducted between the analytical and experimental approaches, and are shown in Fig. 8. The yarn is set to slide with a constant displacement, a sliding distance of 7.5 mm in the forward and backward directions based on the dissimilar β, to complete one friction cycle. The friction force during the friction test can be divided into decreasing (I and III) and increasing phases (II and IV), as shown in Fig. 8a. It can be noted that the change in friction force is significantly different in each phase. It is probably due to the sliding velocity between two contact yarns. The variation in relative parameters will occur if the friction is carried out under the condition of acceleration. Therefore, it also reflects the fact that friction has a rate correlation, as described in Fig. 8b.

To ensure the experimental value is stable, the average data are selected after the five friction experiments. The friction force of the analytical model is calculated based on the average value of n and m. A good agreement between the analytical and experimental friction responses can be sighted in Fig. 8a. However, the variation between each characteristic phase shows a rate correlation in Fig. 8c. This is probably related to θ, which influences the arrangement of the fibers on the contact surface. Furthermore, it can be observed that the analytical and experimental curves separate approximately in the decreasing phase, whose average errors are averagely concentrated at about 21.9% (less than the average experimental error of 36.7%). Meanwhile, the average errors in the increasing phase are about 7.2% (less than the average experimental error of 11.8%).

4.2 Friction Behavior Between the Yarns with the Same Twist

As one essential yarn/yarn fiction parameter, the realistic contact area ($A_{r/yarn}$) depends directly on the normal force

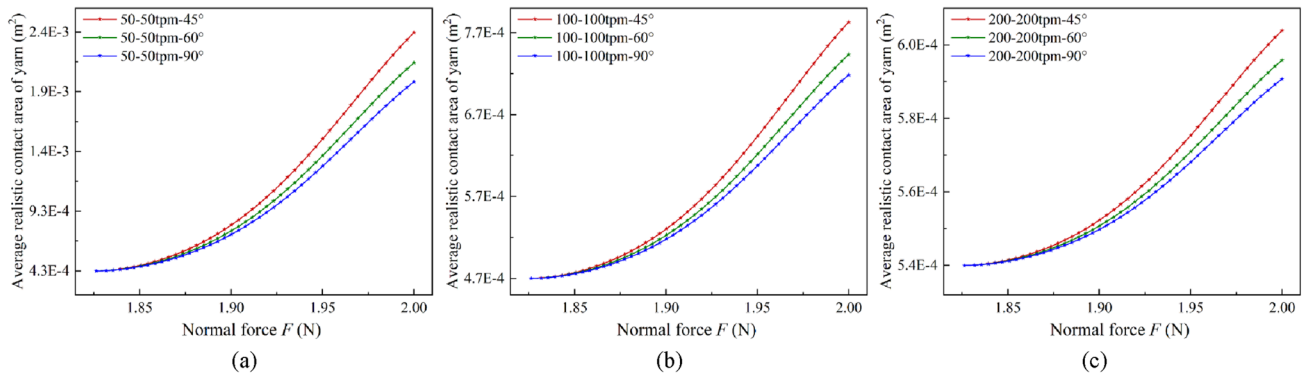

Fig. 9 The realistic contact area of yarn $A_{r/yarn}$ of a typical friction cycle between the yarn: **a** 50 tpm and 50 tpm, **b** 100 tpm and 100 tpm **c** 200 tpm and 200 tpm under the different contact angle. (Note: horizontal comparison: same color in three figures; vertical comparison: three colors in one figure)

applied and is influenced by the yarn twist level and the contact angle between the yarn axes (β). This realistic contact area can be calculated by Eq. (12) and worked out in Fig. 9 in the case of friction between yarns with the same twist. It can be noted that each $A_{r/yarn}$ of yarns almost shows a non-linear relation with an identical tendency towards the normal force, $A_{r/yarn}$ gradually increases as normal force F increases, but the range of variation is dissimilar, which can be explained by Refs. [12, 46]. Among the three twist levels, the biggest range of variation can be observed in the case of 50–50 tpm yarns under horizontal comparison (the twist of upper and lower yarns both are 50 tpm). This phenomenon is probably due to the cohesive force of the fibers as the twist increases with increasing cohesive force, which can be confirmed by the research work presented in [12, 46]. Regarding the contact angle between the yarn axes (β), it is imperative to consider the influence of non-orthogonal yarn configurations ($\beta \neq 90°$), which provide a wider representation of the

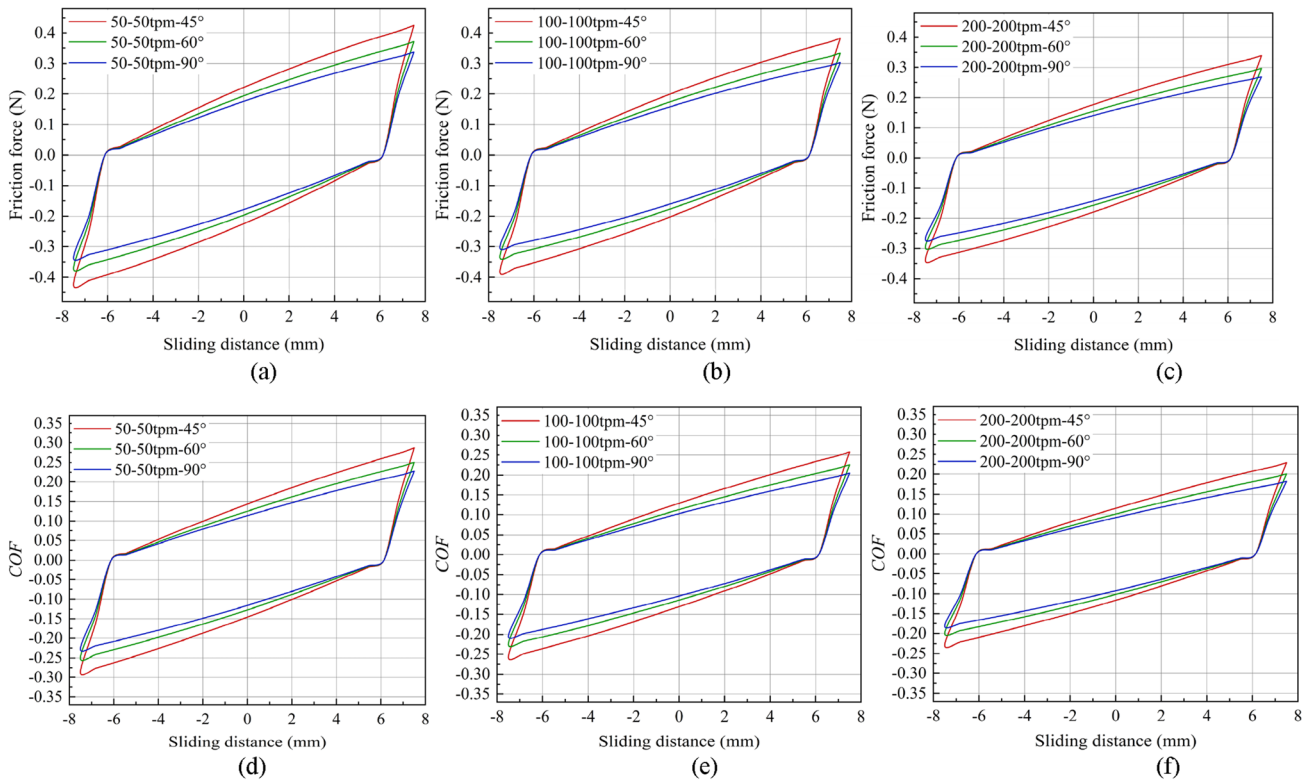

Fig. 10 A typical friction cycle with the same twist: **a–c** friction force and **d–f** *COF*. (Friction condition for test 4 was employed to analyze)

contact area compared to the simplistic scenario of orthogonal yarns ($\beta = 90°$). By incorporating non-orthogonal yarn conditions, a more realistic contact area between yarns can be achieved, leading to a comprehensive understanding of the intricate interplay between yarns geometry and contact behavior. Furthermore, a smaller contact angle β influences a bigger realistic contact area, which can be seen from the different twist levels of curves in Fig. 9a–c.

Based on the realistic contact area between yarns $A_{r/yarn}$, the developed model can predict the friction force F_f and *COF* during the friction test. The friction force and *COF* in the function of the sliding distance in one cycle of friction test between two yarns with the same twist are shown in Fig. 10a–c and in Fig. 10d–f, respectively. A similar variation can be observed between friction force and *COF*. The twist level of yarns and the contact angle between the yarn axes significantly impact the friction force and *COF*. The twist leads to an increase in the compression cohesion force in the circumferential direction of the yarn. Consequently, a higher twist level leads to a dense structure and a smaller contact surface under the same transverse compressive load, which reduces the inter-yarn friction. In addition, the contact angle β changes the realistic contact area of the yarns, with a bigger contact angle generating a smaller realistic contact area on the yarns and a weaker friction force as well as *COF*. However, these influences on the friction force and *COF* can be noted in the stable friction stages (the sliding velocity remains constant in stages II and IV shown in Fig. 8a and b).

4.3 Friction Behavior Between the Yarns with a Different Twist

4.3.1 Yarns with a Different Twist Level and the Same Twist Direction

The analytical model can predict the friction behavior with a different twist, including the twist levels and direction, analogous to Sect. 4.2. Similar relative parameters of friction behavior are selected for analysis. Figure 11 illustrates a more distinguishing trend with different twists in relative parameters. As shown in Fig. 11a–c, the $A_{r/yarn}$ of each twist level calculated by the analytical model is distinct from each other, and the range of variation at the extreme values of the normal force increases with the increasing of twist level. Simultaneously, the range of variation of $A_{r/yarn}$ increases with the increasing span of twist level. With identical twist levels, the $A_{r/yarn}$ of non-orthogonal friction is larger than orthogonal friction under vertical comparison, and there is a marked decrease in $A_{r/yarn}$ as β increases under horizontal comparison due to the tight arrangement of fibers within the larger twist yarn and the greater number of fibers participating in the friction, the frictional behavior of yarn with different twist levels have larger realistic contact area compared to yarns with same twist level.

The evolution of different twist levels on F_f and *COF* is similar to those of the same twist level. In contrast, the range of variation is significant in Fig. 12. For the same β, the 50–00 tpm tends to show a greater range of variation than 100–200 tpm and 150–200 tpm, which may indicate that the span of twist levels plays a role in determining F_f and *COF*. Regarding the comparison of same span of twist level, the ranges of variation of F_f and *COF* decrease with the increasing of β, namely the effect of F_f is significantly greater than F_n with a decreasing span of twist level in Fig. 12a–c and d–f, respectively. Moreover, it is obvious that there is also a phenomenal increase as β drops even though the span of twist level is different. The above influences are also apparent during the stable friction stages.

4.3.2 Yarns with a Different Twist Level and the Different Twist Direction

Figure 13 exhibits the evolution of relative parameters during the friction process with different twist directions. The evolution trend of $A_{r/yarn}$ is also non-linear as is the variation in F, with both expressing an invariant law that

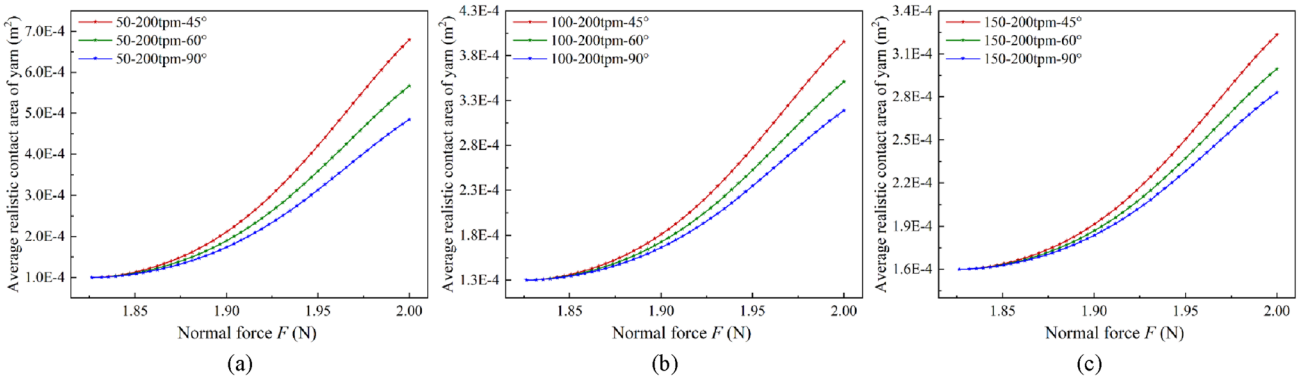

Fig. 11 The realistic contact area of yarn $A_{r/yarn}$ of a typical friction cycle between the yarns: **a** 50 tpm and 200 tpm, **b** 100 tpm and 200 tpm **c** 150 tpm and 200 tpm of same twist direction under different contact angle

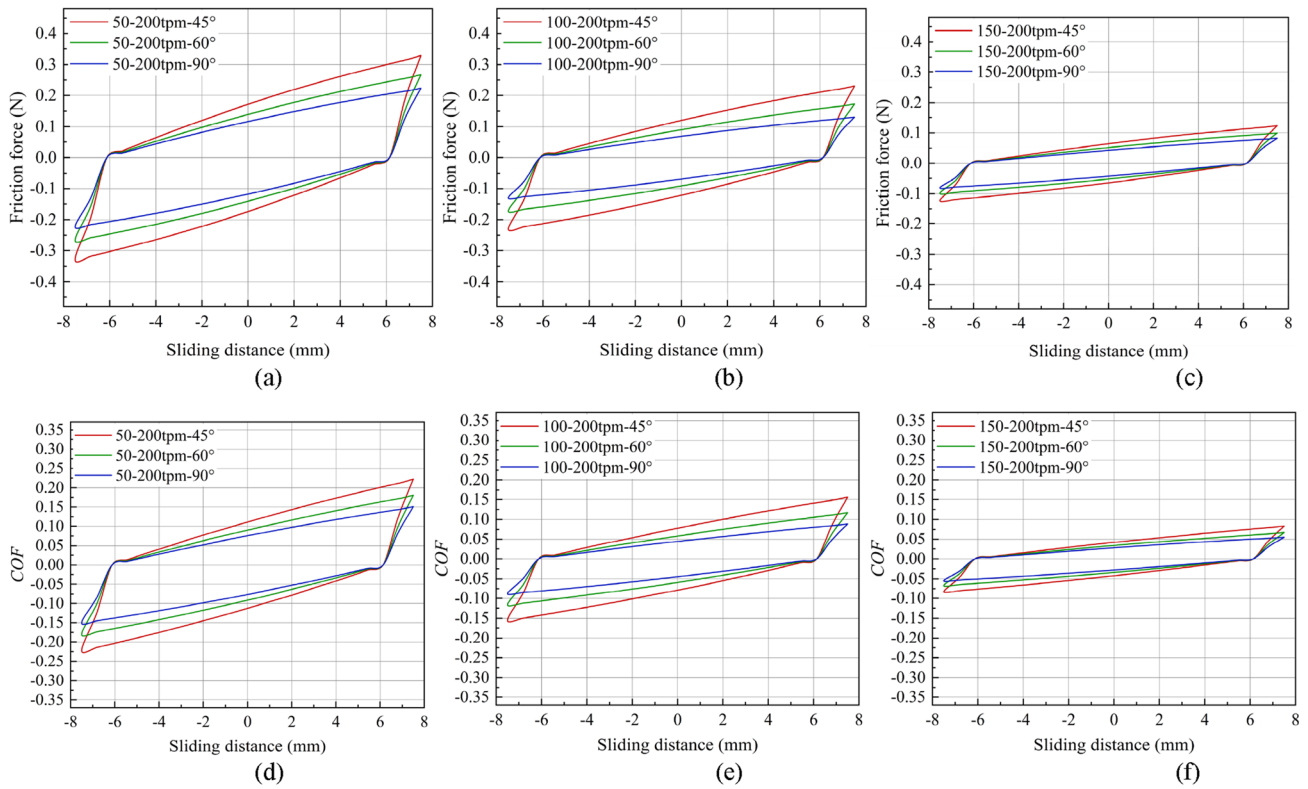

Fig. 12 A typical friction cycle with the different twist levels: **a**–**c** friction force and **d**–**f** *COF*. (Friction condition for test 4 was employed to analyze)

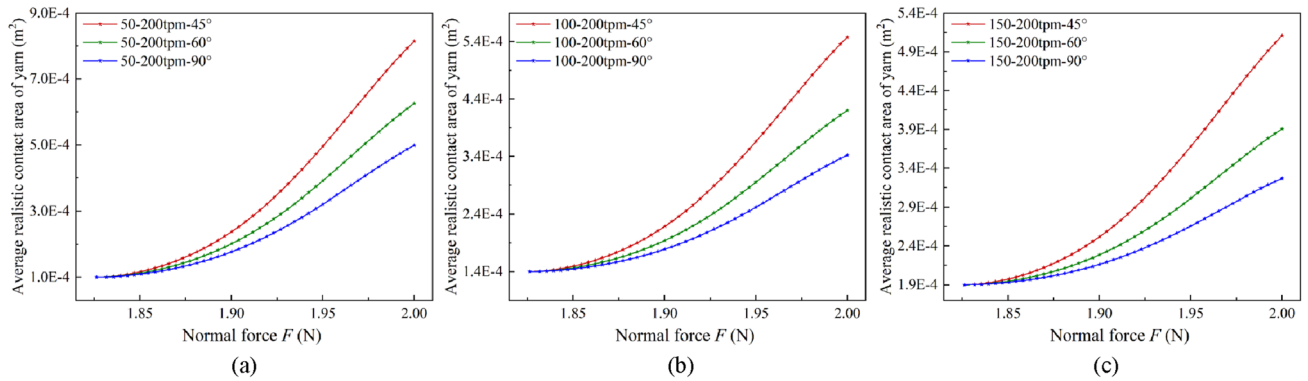

Fig. 13 The realistic contact area of yarn $A_{r/yarn}$ of a typical friction cycle between the yarns: **a** 50 tpm and 200 tpm, **b** 100 tpm and 200 tpm **c** 150 tpm and 200 tpm of different twist direction under different contact angle

the maximum F occurs in the middle position, while the minimum F occurs in transformation positions of direction. And there is no change for $A_{r/yarn}$ at any β in transformation positions of direction, while the change is significant at the position of maximum F with the same span of twist level. The $A_{r/yarn}$ of non-orthogonal friction is larger than orthogonal friction with the same β under horizontal comparison. Additionally, Fig. 13a–c shows the rate of change is insignificant at an F of 2.0 N between 100–200 tpm-45° and 150–200 tpm-45°, while the rate of change of 50–200 tpm-45° is about three times as large as 100–200 tpm-45°, and the evolution is similar to the $A_{r/yarn}$ with same twist direction (Sect. 4.3.1). However, the range of $A_{r/yarn}$ is obviously indicated due to the different calculations of α. Therefore, it has commonly been assumed that the rate of change in $A_{r/yarn}$ increases with increasing span of twist under horizontal comparison, which is available regardless of whether

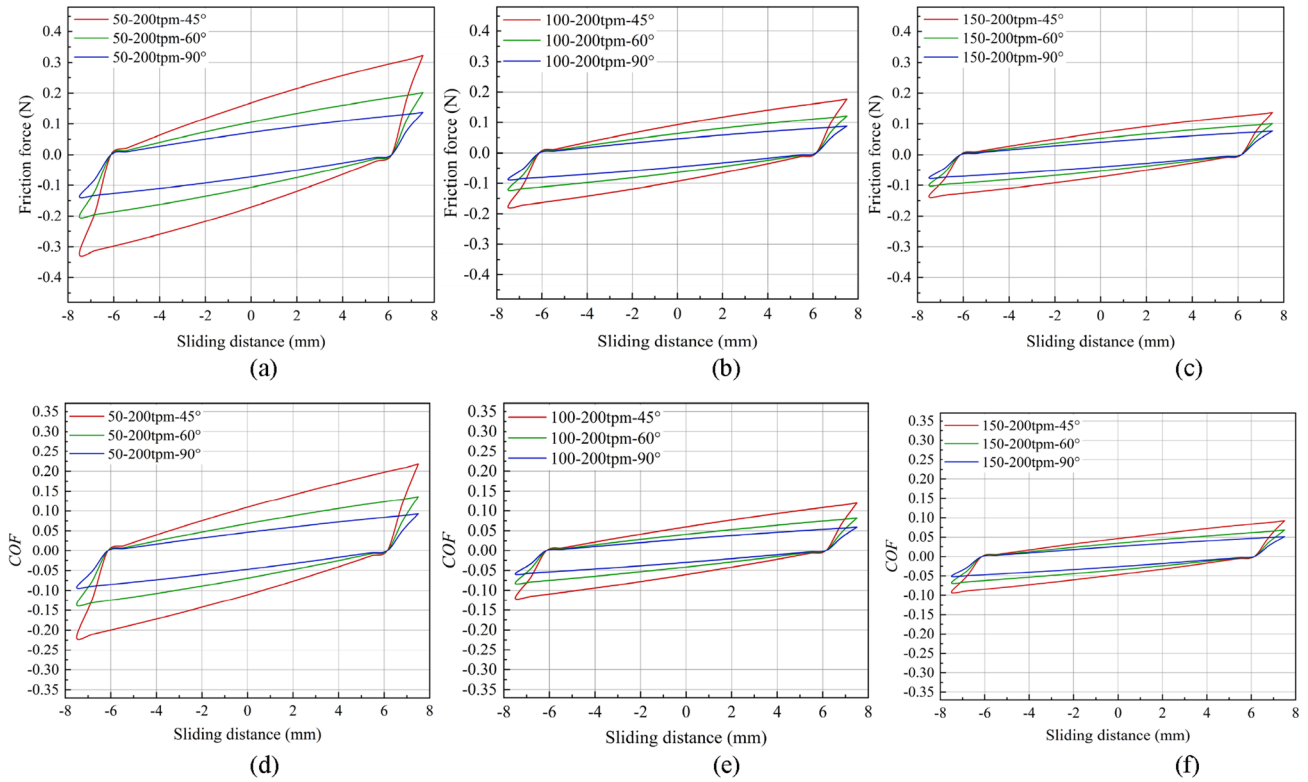

Fig. 14 A typical friction cycle with the different twist directions: **a–c** friction force and **d–f** *COF*. (Friction condition for test 4 was employed to analyze)

it is orthogonal or non-orthogonal. Under the same span of twist level under vertical comparison, a smaller β influences a bigger $A_{r/yarn}$, which can be seen from the three β in each figure (Fig. 13a–c).

Figure 14a–c shows the evolution of yarn friction force during the friction process. This friction force can characterize the friction behavior of yarns with different twist directions, that is, S–Z or Z–S. The span of twist level increases with the increasing range of friction force. The rate of change under a normal force applied of 2.00 N is more significant than other normal forces and is influenced by $A_{r/yarn}$. There is a gradual fall in the range of friction force as β increases, regardless of the span of twist level. Additionally, the trends of *COF* calculated by Eq. (16) are shown in Fig. 14d–f, and are similar to the friction force. However, the rates of change of *COF* and frictional behavior reflected by *COF* are different. For different spans of twist level, it can be revealed that the range of friction force decreases with the decreasing span of twist level during the friction process. The *COF* rises to a high point and peaks at a normal force applied of 2.00 N, which increases with the decreasing of β. In general, the friction behavior is variable regardless of whether the twist is the same or different. The key parameters must thus be considered throughout the friction analysis of yarns.

5 Conclusion

In this research, an analytical model based on Hertzian contact theory at the micro–meso scale was constructed to characterize and predict the relative parameters during the yarn–yarn friction process. On account of the experimental analysis of the friction behavior between non-orthogonal twisted yarns (split into four characteristic phases) and the average error of friction force, the correctness of this model was determined. Furthermore, the analytical model has the ability to predict the friction behavior of yarns with the same and different twists regardless of the contact angle between the yarn axes.

In the same twist friction case, regardless of whether the yarns have similar twist levels and directions, the realistic contact area has an uptrend with the increase in normal load. By contrast, in the different twist friction case (different twist level and twist direction), the increase in relative parameters follows the same pattern as same twist level friction. Regarding β of 45°, 60°, and 90°, a smaller contact angle β influences a bigger realistic contact area. The range of friction force and *COF* increases gradually with the increasing span of twist level regardless of the β. Additionally, the extreme values of the non-orthogonal friction force and *COF* are higher than the corresponding values for orthogonal friction

under the same conditions since the realistic contact area of yarn $A_{r/yarn}$ increases.

The investigation of yarn friction in fiber-reinforced composites assumes paramount importance, as it serves as a critical factor for the optimization of the intricate textile preform forming process, while concurrently enhancing the mechanical performance of the resulting composite materials. Nevertheless, the effects are likely to deviate considerably from the practical situation as a result of the adhesion process. Quantification of the effect of this mechanism on friction behavior requires the development of a numerical model, which will be established based on the present model. Moreover, the question of whether such a model might adequately explain the effect of wear, or the size of the yarns is an intriguing problem for future research.

Appendix A

The changing relationships between θ and displacement H under the action of F are detailed in this appendix. All parameters are shown in Fig. 15. The applied normal force F in the kinematic friction process can be further calculated by tension acting on the lower yarn T through the following equations:

$$T = E_l S\left(\frac{H}{\sin\theta_1} + \frac{H}{\sin\theta_2} - 1\right) + F_p, \tag{17}$$

where E_l is the longitudinal modulus of yarn, S is the area of yarn's cross section, and F_p is the initial pre-tension applied to yarn.

$$\sqrt{(\frac{a}{2} - u)^2 + H^2} + \sqrt{(\frac{a}{2} + u)^2 + H^2} = l, \tag{18}$$

where l is the length of the yarn sample involved in friction which is obtained from the experiment. Moreover, θ_1 and θ_2 are given as

$$\theta_1 = \arctan\frac{2H}{a - l\sqrt{\frac{a^2+4H^2-l^2}{a^2-l^2}}}, \tag{19}$$

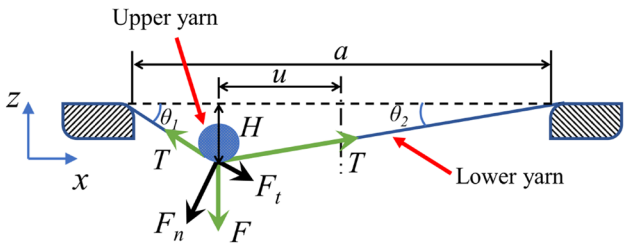

Fig. 15 The description of dimensional parameters during the friction process based on Fig. 5

$$\theta_2 = \arctan\frac{2H}{a + l\sqrt{\frac{a^2+4H^2-l^2}{a^2-l^2}}}, \tag{20}$$

where H is displacement under the action of F, which can have a relationship using θ_1 and θ_2 see Eq. (14):

Acknowledgements The authors gratefully acknowledge: the financial support from the China Scholarship Council (CSC 202108120054).

Author Contributions YW: investigation, methodology, theoretical analysis, experimental analysis, validation, visualization and writing—original draft. YJ: project administration, supervision, validation and review & editing. PW: project administration, supervision, methodology, formal analysis, validation and writing—review & editing.

Data Availability The raw and experimental data required to reproduce these studies can be shared on request.

Declarations

Conflict of interest The authors declare that they have no known competing financial interests or personal relationships that could have appeared to influence the work reported in this paper.

References

1. Xie, J., Guo, Z., Shao, M., Zhu, W., Jiao, W., Yang, Z., Chen, L.: Mechanics of textiles used as composite preforms: a review. Compos. Struct. **304**, 116401 (2023). https://doi.org/10.1016/j.compstruct.2022.116401
2. Gao, Z., Chen, L.: A review of multi-scale numerical modeling of three-dimensional woven fabric. Compos. Struct. **263**, 113685 (2021). https://doi.org/10.1016/j.compstruct.2021.113685
3. Xiao, S., Gao, H., Soulat, D., Wang, P.: A revised model of kinematic analysis on in-plane shearing behaviour of biaxial fabrics in bias extension test. Composites A (2022). https://doi.org/10.1016/j.compositesa.2022.107251
4. Gnaba, I., Legrand, X., Wang, P., Soulat, D.: Through-the-thickness reinforcement for composite structures: a review. J. Ind. Text. **49**, 71–96 (2019). https://doi.org/10.1177/1528083718772299
5. Li, M., Wang, P., Boussu, F., Soulat, D.: A review on the mechanical performance of three-dimensional warp interlock woven fabrics as reinforcement in composites. J. Ind. Text. **51**, 1009–1058 (2022). https://doi.org/10.1177/1528083719894389
6. Yang, Z., Jiao, Y., Xie, J., Chen, L., Jiao, W., Li, X., Zhu, M.: Modeling of 3D woven fibre structures by numerical simulation of the weaving process. Compos. Sci. Technol. **206**, 108679 (2021). https://doi.org/10.1016/j.compscitech.2021.108679
7. Hui, C., Wang, P., Legrand, X.: Improvement of tufting mechanism during the advanced 3-dimensional tufted composites manufacturing: to the optimisation of tufting threads degradation. Compos. Struct. **220**, 423–430 (2019). https://doi.org/10.1016/j.compstruct.2019.04.019
8. Wang, Y., Jiao, Y., Wu, N., Xie, J., Chen, L., Wang, P.: An efficient virtual modeling regard to the axial tensile and transverse compressive behaviors of the twisted yarns. J. Ind. Text. **52**, 15280837221137352 (2022). https://doi.org/10.1177/15280837221137353
9. Simon, J., Hamila, N., Binetruy, C., Comas-Cardona, S., Masseteau, B.: Design and numerical modelling strategy to form tailored

fibre placement preforms: application to the tetrahedral part with orthotropic final configuration. Composites A **158**, 106952 (2022). https://doi.org/10.1016/j.compositesa.2022.106952
10. Wang, Y., Li, X., Xie, J., Wu, N., Jiao, Y., Wang, P.: Numerical and experimental investigation on bending behavior for high-performance fiber yarns considering probability distribution of fiber strength. Textiles **3**, 129–141 (2023). https://doi.org/10.3390/textiles3010010
11. Abtew, M.A., Boussu, F., Bruniaux, P., Loghin, C., Cristian, I., Chen, Y., Wang, L.: Yarn degradation during weaving process and its effect on the mechanical behaviours of 3D warp interlock p-aramid fabric for industrial applications. J. Ind. Text. (2020). https://doi.org/10.1177/1528083720937288
12. Hemmer, J., Lectez, A.-S., Verron, E., Lebrun, J.-M., Binetruy, C., Comas-Cardona, S.: Influence of the lateral confinement on the transverse mechanical behavior of tows and quasi-unidirectional fabrics: experimental and modeling investigations of dry through-thickness compaction. J. Compos. Mater. **54**, 3261–3274 (2020). https://doi.org/10.1177/0021998320912809
13. Cornelissen, B., de Rooij, M.B., Rietman, B., Akkerman, R.: Frictional behaviour of high performance fibrous tows: a contact mechanics model of tow–metal friction. Wear **305**, 78–88 (2013). https://doi.org/10.1016/j.wear.2013.05.014
14. Abu Obaid, A., Gillespie, J.: Effects of abrasion on mechanical properties of Kevlar KM2-600 and S glass tows. Text. Res. J. **89**, 989–1002 (2019). https://doi.org/10.1177/0040517518760753
15. Archer, E., Buchanan, S., McIlhagger, A., Quinn, J.: The effect of 3D weaving and consolidation on carbon fiber tows, fabrics, and composites. J. Reinf. Plast. Compos. **29**, 3162–3170 (2010). https://doi.org/10.1177/0731684410371405
16. Smerdova, O., Benchekroun, O., Brunetiere, N.: Transversal friction of epoxy-lubricated and dry carbon tows: from initial stages to stabilised state. Composites A **143**, 106263 (2021). https://doi.org/10.1016/j.compositesa.2020.106263
17. Gupta, B.S.: Friction in textile materials. Elsevier, Amsterdam (2008)
18. Dackweiler, M., Hagemann, L., Coutandin, S., Fleischer, J.: Experimental investigation of frictional behavior in a filament winding process for joining fiber-reinforced profiles. Compos. Struct. **229**, 111436 (2019). https://doi.org/10.1016/j.compstruct.2019.111436
19. Sugimoto, Y., Shimamoto, D., Hotta, Y.: Evaluation of kinetic friction coefficients between single carbon fibers. Carbon **167**, 264–269 (2020). https://doi.org/10.1016/j.carbon.2020.06.010
20. Engelfried, M., Aichele, B., Middendorf, P.: Investigation of the friction between dry and wetted carbon filaments. Procedia Manuf. **47**, 60–64 (2020). https://doi.org/10.1016/j.promfg.2020.04.130
21. Cornelissen, B., Sachs, U., Rietman, B., Akkerman, R.: Dry friction characterisation of carbon fibre tow and satin weave fabric for composite applications. Composites A **56**, 127–135 (2014). https://doi.org/10.1016/j.compositesa.2013.10.006
22. Mulvihill, D.M., Sutcliffe, M.P.F.: Effect of tool surface topography on friction with carbon fibre tows for composite fabric forming. Composites A **93**, 199–206 (2017). https://doi.org/10.1016/j.compositesa.2016.10.017
23. Roselman, I.C., Tabor, D.: The friction and wear of individual carbon fibres. J. Phys. Appl. Phys. **10**, 1181–1194 (1977). https://doi.org/10.1088/0022-3727/10/8/018
24. Xiang, Z., Liu, Y., Zhou, X., Wu, Z., Hu, X.: Interlayer contact mechanism of the frictional behavior of glass-fiber woven fabrics and improvements of winding characteristics. Compos. Struct. **233**, 111497 (2020). https://doi.org/10.1016/j.compstruct.2019.111497
25. Shanwan, A., Gassara, H.-E., Barbier, G., Sinoimeri, A.: New experimental device for measuring the inter-fiber transversal friction. IOP Conf. Ser. Mater. Sci. Eng. **254**, 142020 (2017). https://doi.org/10.1088/1757-899X/254/14/142020
26. Gassara, H.E., Barbier, G., Wagner Kocher, C., Sinoimeri, A., Pumo, B.: Experimental evaluation of transverse friction between fibers. Tribol. Int. **119**, 112–122 (2018). https://doi.org/10.1016/j.triboint.2017.10.035
27. Tourlonias, M., Bueno, M.-A., Jordan, C., Poquillon, D.: Influence of wear on the sizing layer and desizing of single carbon fibre-to-fibre friction. Wear **402–403**, 64–70 (2018). https://doi.org/10.1016/j.wear.2018.02.003
28. Smerdova, O., Sutcliffe, M.P.F.: Multiscale tool–fabric contact observation and analysis for composite fabric forming. Composites A **73**, 116–124 (2015). https://doi.org/10.1016/j.compositesa.2015.03.009
29. Tourlonias, M., Bueno, M.-A.: Experimental simulation of friction and wear of carbon yarns during the weaving process. Composites A **80**, 228–236 (2016). https://doi.org/10.1016/j.compositesa.2015.07.024
30. Salem, M.M., De Luycker, E., Delbe, K., Fazzini, M., Ouagne, P.: Experimental investigation of vegetal and synthetic fabrics cohesion in order to prevent the tow sliding defect via frictional and pull-out test. Composites A **139**, 106083 (2020). https://doi.org/10.1016/j.compositesa.2020.106083
31. Ismail, N., de Rooij, M.B., de Vries, E.G., Zini, N.H.M., Schipper, D.J.: Friction between single aramid fibres under pre-tension load. Tribol. Int. **137**, 236–245 (2019). https://doi.org/10.1016/j.triboint.2019.04.013
32. Roselman, I.C., Tabor, D.: The friction of carbon fibres. J. Phys. Appl. Phys. **9**, 2517 (1976). https://doi.org/10.1088/0022-3727/9/17/012
33. Howell, H.G., Mazur, J.: Amontons' law and fibre friction. J. Text. Inst. Trans. **44**, T59–T69 (1953). https://doi.org/10.1080/19447025308659728
34. Bowden, F.P., Leben, L.: The nature of sliding and the analysis of friction. Proc. R. Soc. Lond. Ser. Math. Phys. Sci. **169**, 371–391 (1939). https://doi.org/10.1098/rspa.1939.0004
35. He, C., Ge, J., Chen, Y., Lian, Y.: Concurrent multiscale virtual testing for 2D woven composite structures: a pathway towards composites design and structure optimization. Compos. Struct. (2022). https://doi.org/10.1016/j.compstruct.2022.116406
36. Wu, N., Xie, X., Yang, J., Feng, Y., Jiao, Y., Chen, L., Xu, J., Jian, X.: Effect of normal load on the frictional and wear behaviour of carbon fiber in tow-on-tool contact during three-dimensional weaving process. J. Ind. Text. (2020). https://doi.org/10.1177/1528083720944615
37. Tourlonias, M., Bueno, M.-A., Fassi, G., Aktas, I., Wielhorski, Y.: Influence of friction angle between carbon single fibres and tows: experimental analysis and analytical model. Composites A **124**, 105478 (2019). https://doi.org/10.1016/j.compositesa.2019.105478
38. Tourlonias, M., Bueno, M.-A., Poquillon, D.: Friction of carbon tows and fine single fibres. Composites A **98**, 116–123 (2017). https://doi.org/10.1016/j.compositesa.2017.03.017
39. Li, M., Wang, P., Boussu, F., Soulat, D.: Investigation of impact performance of 3-dimensional interlock polymer fabrics in double and multi-angle pass stabbing. Mater. Des. **206**, 109775 (2021). https://doi.org/10.1016/j.matdes.2021.109775
40. He, Y., Jiao, Y., Zhou, J.Q., Lei, H., Jia, N., Chen, L., Zhang, D.: Ballistic response of ultra-high molecular weight polyethylene laminate impacted by mild steel core projectiles. Int. J. Impact Eng. **169**, 104338 (2022). https://doi.org/10.1016/j.ijimpeng.2022.104338
41. Bazan, P., Mierzwiński, D., Bogucki, R., Kuciel, S.: Bio-based polyethylene composites with natural fiber: mechanical, thermal, and ageing properties. Materials **13**, 2595 (2020). https://doi.org/10.3390/ma13112595

42. Han, L., Cai, H., Chen, X., Zheng, C., Guo, W.: Study of UHMWPE fiber surface modification and the properties of UHMWPE/epoxy composite. Polymers **12**, 521 (2020). https://doi.org/10.3390/polym12030521
43. Popov, V.L.: Rigorous treatment of contact problems—hertzian contact. In: Popov, V.L. (ed.) Contact mechanics and friction: physical principles and applications, pp. 57–81. Springer, Berlin (2017)
44. Kawabata, S.: Measurement of the transverse mechanical properties of high-performance fibres. J. Text. Inst. **81**, 432–447 (1990). https://doi.org/10.1080/00405009008658721
45. Walther, J., Bessette, C., Decrette, M., Tourlonias, M., Bueno, M.-A., Osselin, J.-F., Charleux, F., Coupé, D.: Yarn damage conditions due to interactions during interlock weaving process: in-situ and in-lab experiments. Appl. Compos. Mater. **29**, 245–262 (2022). https://doi.org/10.1007/s10443-021-09950-7
46. Daelemans, L., Tomme, B., Caglar, B., Michaud, V., Van Stappen, J., Cnudde, V., Boone, M., Van Paepegem, W.: Kinematic and mechanical response of dry woven fabrics in through-thickness compression: virtual fiber modeling with mesh overlay technique and experimental validation. Compos. Sci. Technol. **207**, 108706 (2021). https://doi.org/10.1016/j.compscitech.2021.108706